Epitactic magnetite growth in fluid inclusions as driving force for olivine oxidation coupled with hydrogen production at high pressure

N. Malaspina[1*], M. Campione[1], S. Tumiati[2], M. Murri[1], P. Fumagalli[2], V. Cerantola[1], M. La Fortezza[3], M. Scambelluri[3]

[1*] Dipartimento di Scienze dell'Ambiente e del Territorio e di Scienze della Terra, Università degli Studi di Milano-Bicocca, Piazza della Scienza 4, 20126 Milano, Italy (nadia.malaspina@unimib.it; marcello.campione@unimib.it; mara.murri@unimib.it; valerio.cerantola@unimib.it)

[2] Dipartimento di Scienze della Terra, Università degli Studi di Milano, via Mangiagalli 34, 20133 Milano, Italy

[3] Dipartimento di Scienze della Terra (simone.tumiati@unimi.it; patrizia.fumagalli@unimi.it) dell'Ambiente e della Vita, Università degli Studi di Genova, Corso Europa 26, 16132 Genova, Italy (mattia.lafortezza@edu.unige.it; marco.scambelluri@unige.it)

Highlights

- Fluid inclusions in olivine simulate a process of oxidation of the mantle by water.
- H_2O/olivine interaction is governed by magnetite-olivine epitaxy.
- H_2 can be produced under oxidising conditions, driven by epitactic magnetite.
- Olivine may act as a trap for molecular hydrogen at high pressure.

Abstract

We disclose the crystallization evolution of magnetite-bearing multiphase inclusions hosted in metamorphic olivine of harzburgites from the Cerro de Almirez (Betic Cordillera,

Spain), which have been interpreted as final products of the trapping of the aqueous fluid produced by the subduction-zone dehydration of former serpentinites. The chemical exchange between inclusion fluid and olivine started soon after entrapment, at peak *P-T* conditions of 1.6-1.9 GPa and 650-700 °C, and continued during cooling along the retrograde path, with the coexistence of olivine and magnetite with orthopyroxene, chlorite, talc, antigorite and the destabilisation of olivine and antigorite into brucite and low-temperature chrysotile serpentine, as recognised by Raman analyses. Thermodynamic modelling and mass balance calculations demonstrate that the water component of fluid trapped in the inclusions of metamorphic olivine is expected to trigger the oxidation of the fayalite component in olivine, producing a mineral assemblage made of magnetite + orthopyroxene and molecular hydrogen, where the elemental redox processes are Fe^{2+} of olivine that oxidizes to Fe^{3+} and H^{+} of water that reduces to H_2. Probable H_2 trapped in the olivine host close to the inclusion wall has been detected by Raman spectroscopy. To corroborate its presence, we performed quantitative mass spectrometry analyses of the fluid phase trapped in the multiphase inclusions and of the olivine crystals hosting the inclusions, revealing that 1 kilogram of olivine matrix contains 6.2 ± 0.1 mmol of H_2. We identify two synergistic driving forces of the whole process, which has the peculiarity to produce molecular hydrogen at apparently oxidising conditions: i) the building up of an epitaxial interface between olivine and magnetite, and ii) the olivine ability to trap H_2 at high pressures. The olivine + H_2O system of these natural microreactors simulates a process of oxidation of the mantle olivine by water, with production of H_2 at pressure and fO_2 conditions (FMQ+2) at which water reduction is considered an unlike mechanism.

Keywords

Harzburgites, redox reactions, subduction zone fluids, multiphase inclusions, hydrogen

1. Introduction

There is a general consensus that the lithospheric mantle wedge above subduction zones is apparently more "oxidised" (i.e., records higher fO_2) than other mantle domains as a result of metasomatism by slab-derived fluid phases (Brandon and Draper, 1996; Malaspina et al., 2009a; 2010; 2012; Evans et al., 2012; Cannaò and Malaspina, 2018: Cottrell et al., 2021; Tumiati et al., 2022). Nevertheless, the dispute about the process responsible for this relative oxidation and the actual oxidising capacity of slab-derived metasomatic fluids at sub-arc depths is still going on. If pure water itself cannot be assumed as an efficient oxidising agent due to the "vanishingly small" oxygen chemical potential (i.e., fO_2) resulting from the very low H_2O dissociation constant (Frost and Ballhaus, 1998), experimental studies (e.g. Poli, 2015; Tumiati et al., 2013; Iacovino et al., 2020; Maurice et al., 2020; Tiraboschi et al., 2023) and natural occurrences (e.g. Mungall, 2002; Kelley and Cottrell, 2009; Evans, 2012; Malaspina et al., 2012; 2017; Tumiati et al., 2015) demonstrated that slab-derived fluids, hypersaline brines, supercritical liquids or silicate/carbonatitic melts can be efficient carriers of Fe^{3+}, carbonates, sulphates or alkali able to largely oxidise the Fe^{2+} of mantle mineral assemblages.

Among the dehydration reactions occurring in the subducting slab, antigorite breakdown is the most efficient aqueous fluid producer at sub-arch depths, providing up to 13 wt.% of bulk H_2O (Ulmer and Trommsdorff, 1995; Trommsdorff et al., 1998; Scambelluri et al., 2001; 2004; Padrón-Navarta et al., 2011) to the overlying mantle. As summarised by Evans and Frost (2021), thermodynamic modelling and experimental results applied to case studies on the redox state of natural aqueous fluids produced by deserpentinization during subduction point out that they could be oxidised (Debret et al., 2014; Debret and Sverjensky, 2017; Merkulova et al.,

2017; Duan et al. 2022) as well as reduced (Piccoli et al., 2019; Vitale-Brovarone et al., 2020). It must be noted that all these calculations assume that the redox state (in terms of intensive variable fO_2) of the antigorite-breakdown fluid is buffered by the mineral assemblages formed by the dehydration reaction (i.e., variable occurrence of magnetite, hematite, pentlandite or awaruite).

A novel approach to model fluid/mineral interactions employs multiphase fluid inclusions as natural microreactors that can disclose information on the nature and composition of fluids produced at high and ultrahigh pressures and of their interaction with their mineral hosts (e.g., garnet or olivine), treated as simplified solid systems. Inclusions can preserve information on the composition of subduction fluids (Scambelluri et al., 2001; Malaspina et al., 2006; Scambelluri et al., 2015; Frezzotti and Ferrando 2015), the redox budget of the fluid after its interaction with the host (Malaspina et al., 2017; Evans and Tomkins, 2020), or can give information about the textural relations between the host and the daughter minerals from which one can retrieve the kinetics of crystallisation and the fluid/mineral interaction at high and ultrahigh pressures (Malaspina et al., 2015; Campione et al., 2017; Campione et al., 2020). Multiphase inclusions trapped in metamorphic olivine from spinifex-like chlorite harzburgites from Cerro de Almirez (Betic Cordillera, Spain) consist of magnetite-bearing daughter minerals and an aqueous fluid. They have a composition representative of a subduction fluid, enriched in silica, Al_2O_3 and fluid mobile elements that records the geochemical signature of arc magma sources (Scambelluri et al., 2001). These inclusions therefore represent a perfect case study to investigate the water-induced redox metasomatism of mantle olivine near the subduction interface at sub-arc depths (2 GPa and 650 °C), at high fluid/rock ratios. Here we show that water and olivine are involved in a redox reaction which is triggered by the formation of an epitaxial interface between olivine and magnetite crystals

and sustained by the diffusion of the molecular hydrogen produced in high amounts during the process and trapped by the olivine matrix.

2. Petrological background and inclusions description

The rocks presented here are metamorphic spinifex-like chlorite harzburgites associated with meta-rodingites and eclogites that, together with granofels-like chlorite harzburgite, were produced during middle Miocene Alpine subduction by the dehydration of antigorite serpentinite (Trommsdorff et al., 1998; Puga et al., 1999; López Sánchez-Vizcaíno et al., 2001; Padrón-Navarta et al., 2010). At peak conditions of 1.6-1.9 GPa and T = 650-700 °C (López Sánchez-Vizcaíno et al., 2001; Scambelluri et al., 2001; Padrón-Navarta et al., 2010; Bretscher et al., 2018) serpentinite recrystallised to enstatite + olivine + chlorite solid assemblages, accompanied by release of abundant aqueous fluid. The whole process can be described by reaction (Padrón-Navarta et al., 2011):

1 antigorite = 6 olivine + 6 orthopyroxene + 4 chlorite + 15 H_2O (1)

Chlorite harzburgites also show magnetite among the mineral phases (5.8-7.8 wt.%), interpreted by Vieira Duarte et al. (2021) as product mineral of reaction (1).

In the spinifex-like rocks metamorphic olivine shows clear cores and brown pleochroic rims containing sub microscopic magnetite, Cr-spinels and ilmenite + Fe-Cr-Ti-rich oxides (Ruiz-Cruz et al., 1999). These olivines also host primary multiphase inclusions representing the trapped remnant of the fluid produced by reaction (1) (Trommsdorff et al., 1998; Scambelluri et al., 2001). The inclusions contain solid daughter–phase assemblages constituted by olivine, magnetite, ilmenite, chlorite, rare Cl-apatite and interstitial liquid water (Scambelluri et al., 2001). In the studied samples, primary clusters of multiphase inclusions in

the cores of metamorphic olivine (Fig. 1A) show variable inclusion sizes (4 to maximum 20 µm), negative crystal shapes and constant volume proportion of the infilling minerals. Magnetite is systematically present: it occupies up to 30% of the inclusion volumes and crystallised in a peculiar microstructural position at the olivine inclusion wall (Fig. 1B). According to single-crystal X-ray diffraction (Campione et al., 2020), the magnetite(111) plane is systematically parallel to olivine(100) with three symmetrically equivalent relative orientations (Fig. 1C), sharing a precise epitaxial registry. In this configuration the triangular lattice of magnetite is oriented in a way that all its lattice nodes are coincident with the lattice nodes of olivine. This relationship is called "commensurate" and appears as an exceptional occurrence being the strongest and rarest form of lattice match, as evidence of a heterogeneous nucleation of magnetite on olivine.

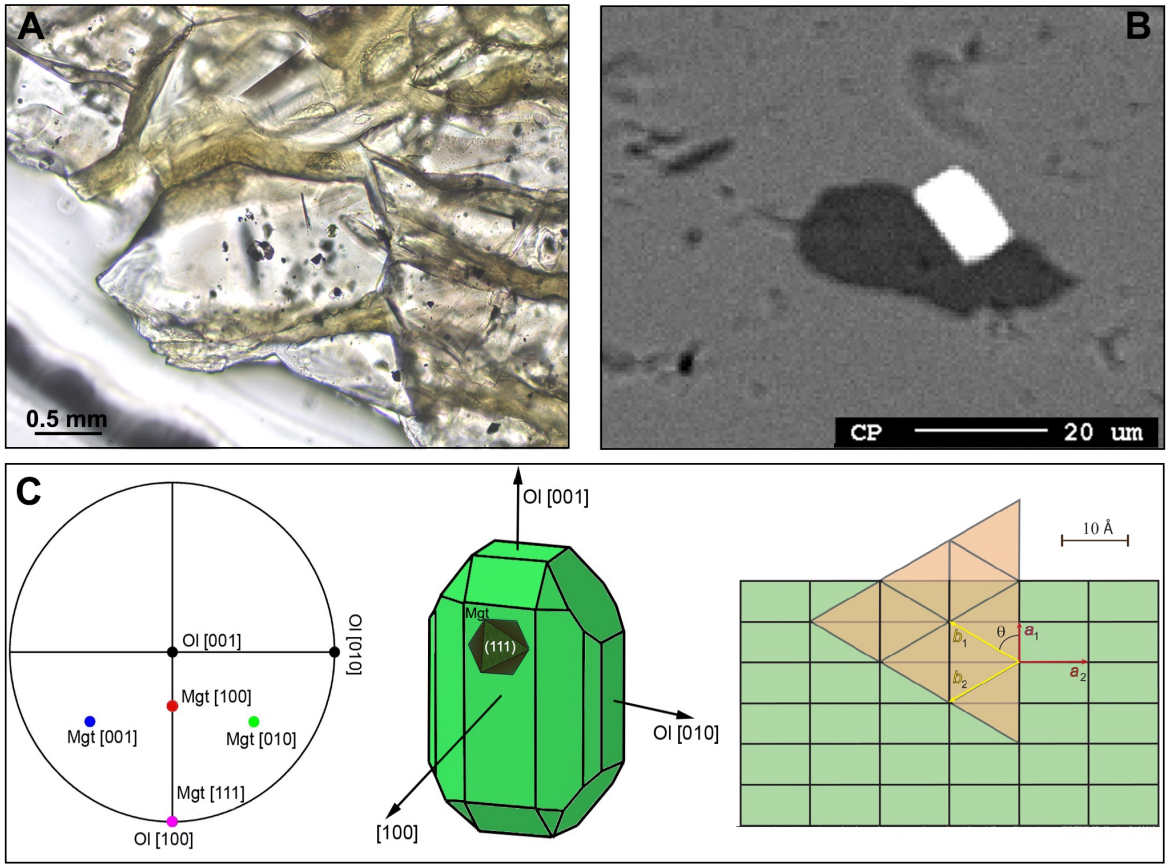

Figure 1: Optical micrograph (A) and back-scattered electron (BSE) image (B) of solid microinclusions in olivine. Magnetite microcrystals with a cubic habit grow in contact with the olivine host mineral showing constant geometric relations with the inclusion's cavity wall. (C) Stereographic projection showing the orientation of magnetite inclusions relative to olivine host

plotted with (100), (010), and (001) planes (black open dots) oriented parallel to the x, y, and z axis, respectively. The magnetite (Mgt) (111) and olivine (Ol) (100) are contact planes with a precise epitaxial registry as shown in the geometric modeling deduced by calculating the lattice mismatch between Mgt(111) (brownish lattice with $b_1 = b_2 = 11.84$ *Å) and Ol(100) (greenish lattice with* $a_1 = 5.98$ *Å and* $a_2 = 10.23$ *Å). Redrawn after Figures 2 and 3 of Campione et al. (2020).*

3. Analytical methods

3.1. Electron microprobe analyses

Major element concentrations of the inclusions' mineral infillings were analysed by wavelength dispersive spectrometry using a Jeol 8200 Super Probe at the Dipartimento di Scienze della Terra, University of Milano and the most representative are reported in Table 1. Acceleration voltage was set to 15 kV, beam sample current was 5 nA and 1 μm beam diameter. Natural standards used were omphacite (Na), grossular (Ca, Al, and Si), fayalite (Fe), olivine (Mg), orthoclase (K), rhodonite (Mn), ilmenite (Ti), niccolite (Ni) and pure Cr (Cr). A counting time of 30 s was used for all elements. A PhiRhoZ routine was used for matrix correction.

3.2. Raman spectroscopy

Micro-Raman spectra were collected with a Horiba Jobin – Yvon Explora_Plus single-monochromator spectrometer with grating of 2400 lines/mm, equipped with an Olympus BX41 microscope at the University of Genova and by means of Horiba LabRam HR Evolution micro-Raman spectrometer at the Dipartimento di Scienze della Terra "A. Desio", University of Milano, equipped with Ultra Low Frequency (ULF) filters. All the spectra were acquired with a green laser (Nd-YAG 532 nm/100mW) focused through a 100× objective (NA aperture = 0.9), giving a spatial resolution of approximately 1 μm and the spectra were calibrated using

168 the 520.7 cm^{-1} line of a silicon wafer. Spectral resolution was 2 cm^{-1} and the instrumental
169 reproducibility in determining the peak positions was ~0.5 cm^{-1}. Raman shifts have been
170 collected in two spectral ranges: one from 100 to 1250 cm^{-1} to determine the stretch of the
171 silicate portion of the phases, and one from 3000 to 3800 cm^{-1} for the OH region. All the
172 analyses were performed setting 20 s as time of acquisition, for 5 accumulations. We only
173 modified these settings when analysing the opaque phases: we set the acquisition time to 180 s
174 and accumulation to 4 accumulations with the laser power at 3-5 mW.
175 Raman mapping has been performed to detect hydrogen. A natural hydrogen inclusion
176 (courtesy from A. Vitale-Brovarone) has been used as reference standard. The spectral range
177 was set from 4000 to 4300 cm^{-1} and the acquisition time was 60 s for 10 accumulations.
178 The OriginPro 2018 software package was used for data evaluation and the collected
179 spectra were baseline corrected for the continuum luminescence background.
180
181 *3.3. Analyses of bulk fluid*
182
183 Hand-picked fragments of olivine from rock sample AL95-64 (1.00 g) and a dozen 3-
184 mm agate grinding balls were put into a 1.5-ml cryogenic vial, which was then flushed with
185 pure Ar to remove air. The vial was closed tightly with its screw cap equipped with a silicone
186 O-ring and sealed at room temperature with epoxy resin. The sealed vial has been shaken with
187 a high-frequency vibrating screen for at least 3 hours, until the rock fragments were converted
188 into a fine-grained, μm-sized powder. To measure the amount and the composition of the fluid
189 phase liberated during this grinding process, we employed a modified version of the capsule-
190 piercing technique (Tiraboschi et al., 2016), where experimental capsule is replaced by the
191 cryogenic vial. Fluids are extracted by piercing the vial in a Teflon extraction vessel (reactor),
192 heated by an electric furnace to ~90 °C (i.e., below the decomposition temperature of any

hydrous phase) to convert liquid water into water vapor. Then, fluids were conveyed into a quadrupole mass spectrometer (QMS) using ultrapure argon (Ar) as the carrier gas. The QMS was connected to the reactor by a heated line (~90 °C) to avoid water vapor condensation on metal tubes. Pressures in the reactor were measured by a high-resolution sensor gauge, with an accuracy of ± 1 mbar. Temperatures in the reactor were monitored by a K-type thermocouple. The internal volume of the reactor was constrained based on the distance between its base and top parts. Thus, the total moles of gases (n) released from the vial were retrieved using the ideal gas law $n = \Delta P \cdot V/(R \cdot T)$, where ΔP is the pressure increase in the reactor after piercing, V is the volume of the reactor, R is the gas constant, and T is the temperature in the reactor during piercing. During the QMS analysis, selected mass/charge (m/z) channels were monitored to measure the fluid species. The QMS calibration was performed using double-distilled water (typically 1 µL) and three gas mixtures with known compositions (80 vol% Ar + 10 vol% CO_2 + 10 vol% O_2, 80 vol% Ar + 10 vol% CH_4 + 10 vol% CO, and 90 vol% Ar + 10 vol% H_2). The calibration enables the retrieval of micromoles (µmol) of H_2O, CH_4, CO_2, CO, H_2, and O_2, with uncertainties of ~1 mol% for all the species except for CO (~10 mol%) due to the interference of atmospheric N_2 on the 28 m/z channel (Tumiati et al., 2017). When the fluid products are transferred into the QMS, micromolar concentrations of volatile molecular species are obtained by comparing the integrated fragmentation peaks of characteristic m/z channels with those of the calibration gases, considering all possible interferences using a least squares regression method (Tiraboschi et al., 2016). Monte Carlo simulations provided the propagation of uncertainties for the COH fluid species, corresponding to their measurement uncertainties. A blank control measurement has been performed by piercing a vial prepared following the procedure outlined above, but without the addition of rock fragments (Table 2).

3.4. Synchrotron Mossbauer spectroscopy

We measured more than 20 micro-magnetite inclusions distributed in two rock thin sections and the corresponding olivine host. Some analyses of olivine have been performed in sites free from inclusions. We collected Synchrotron Mossbauer Spectroscopy (SMS) spectra at ID18, the nuclear resonance beamline of the European Synchrotron Radiation Facility (ESRF). Synchrotron Mössbauer in energy domain is possible using an iron borate ($^{57}FeBO_3$) single crystal, kept close to its Néel temperature and which vibrate parallel to the incident and outgoing X-ray beam at typical Mössbauer velocities up to 15 mm s^{-1} (Potapkin et al., 2012; Rüffer and Chumakov, 1996). In contrast to common radioactive sources, the radiation generated by the SMS is a needle-like collimated beam with mm-size, which can be further focused to spot sizes of micrometric lateral and vertical dimensions and is fully polarized and recoilless. The experiments were carried out at ambient conditions with Be lenses used to collimate the X-ray beam before the $^{57}FeBO_3$ crystal nuclear monochromator and at velocities of ± 12 mm s^{-1} calibrated using a 25 μm thick natural α-iron foil. The X-ray beam-size was 9 (vertical) × 4 (horizontal) μm^2. The linewidth of the source was controlled before and after each sample measurement using the standard $K_2Mg[^{57}Fe(CN)_6]$, whose Mössbauer spectrum consists of a single line at ambient conditions. The data were then fitted with the software *MossA* using the full transmission integral and a Lorentzian-squared source line shape (Prescher et al., 2012). The SMS spectrum at room temperature of magnetite inclusions is given by the contribution of the magnetite phase itself together with that of the olivine host. The magnetite spectrum consists of two partially overlapped Zeeman splitted sextets. One sextet is assigned to tetrahedrally coordinated Fe^{3+} (sites "A", isomer shift 0.27 mm s^{-1}, negligible quadrupole splitting, hyperfine field close to 49 T). The other sextet (isomer shift 0.67 mm s^{-1}, negligible quadrupole splitting, hyperfine field 46 T) is assigned formally to $Fe^{2.5+}$ in octahedral environment, due to fast (10 ns << nuclear Larmor precession time) electron exchange between

243 octahedral Fe^{2+} and Fe^{3+} (sites "B") (Lyubutin et al., 2009). The olivine spectrum consists of
244 two doublets corresponding to the two octahedrally coordinated Fe^{2+} crystallographic sites: *M*1
245 and *M*2. However, in a few measurements Fe^{3+} has also been detected in olivine, which results
246 in an additional doublet with isomer shift close to 0.35 mm s^{-1} and a quadrupole splitting
247 between 0.5 and 0.7 mm s^{-1} in the SMS spectra. All the chemical physical parameters extracted
248 from the fitting of SMS spectra are reported in the supplementary material of Campione et al.
249 (2022). We reported in Table 1 and Figure 6 the $Fe^{3+}/\Sigma Fe$ of the magnetite inclusions shown in
250 Figure 3.
251
252 *3.5. Thermodynamic modelling*
253
254 We calculated log fO_2–*P*-*T* section along a retrograde *P*-*T* path and a log fO_2–log fH_2
255 diagram at peak conditions of 1.6 GPa and 670 °C (*P*–*T* estimates after Bretscher et al., 2018)
256 in the MgO + FeO + SiO_2 + H_2O + O_2 system, for a fixed bulk composition (MgO = 48.81 wt%,
257 SiO_2 = 40.69 wt%, FeO = 9.94 wt%) corresponding to pure Almirez olivine (Olivine in Table
258 1; X_{Mg} = 90), at water saturation conditions, employing the Perple_X software package (version
259 6; Connolly, 2005). We used the internally consistent thermodynamic database of Holland and
260 Powell (1998) revised in 2004 (hp04ver.dat) and the following solid solution models: olivine,
261 orthopyroxene and cummingtonite, (Holland and Powell, 1998), wustite (Fabrichnaya 1999),
262 ferropericlase (Holland et al., 2013) and antigorite (Padrón-Navarta et al., 2013). Anthophyllite
263 (orthoamphibole), clinohumite, brucite and talc were treated as ideal solid solutions between
264 Fe- and Mg end-members. Aqueous fluid phase in the log fO_2–log fH_2 diagram was described
265 by a generic hybrid H_2O–H_2–O_2 fluid EoS (Modified Redlich-Kwong – MRK – by Pitzer and
266 Sterner, 1994), which is in the routine "fluids" of Perple_X package. With this EoS, we
267 calculated the fO_2 and fH_2 resulting from the dissociation of pure water [X_O = O/(H+O)molar

= ~ 1/3) at the P–T of interest. fO_2 and fH_2 were then used to draw the blue line in Figure 8, representing the locus of points where water is stable (or, in other words, where the fO_2 and fH_2 are buffered by water dissociation) (cf. also Peng et al., 2021). The fayalite + magnetite + quartz (FMQ) buffer is shown for reference. The build file is available in the supplementary material.

Despite the occurrence of Al-bearing phases in the multiphase inclusions (e.g., chlorite or antigorite) due to the enrichment of Al_2O_3 in the fluid produced by the dehydration of antigorite (Scambelluri et al., 2001), we modelled a simplified system where olivine reacts with pure water, given that the addition of Al_2O_3 as a component in the bulk does not represent the fluid composition and does not change the stability of the phase assemblages.

3.6. Methodology of magnetite molar volume calculation

We estimated the moles of magnetite contained in 117 mg of sample Al9564 in order to verify the stoichiometric ratio 1:1 between moles of magnetite and moles of hydrogen produced by reaction:

$$3\ Fe_2SiO_4 + H_2O \rightarrow Fe_3O_4 + 3\ FeSiO_3 + H_2 \quad (2)$$

The estimate has been calculated by measuring the maximum plane-projected length of 142 magnetite crystals observed in thin section pictures, performing an image analysis with the ImageJ software (Fig. 2).

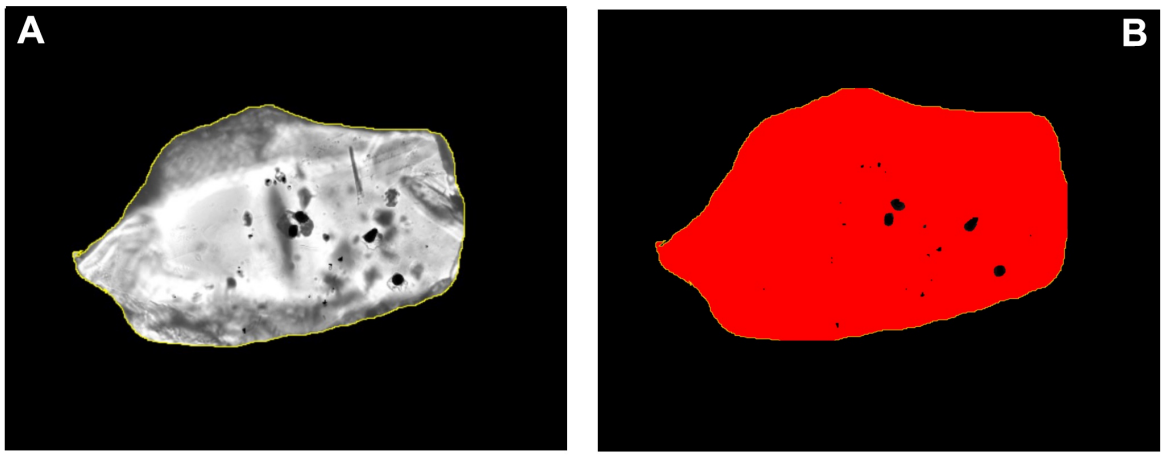

Figure 2: (A) Selected olivine crystal for image analysis. (B) Example of image processing to calculate the maximum plane-projected length of magnetite crystals (black) inside the olivine matrix (red).

Assuming that magnetite can be represented by a cube of parameter a, the maximum linear size of a cube projected in 2D lies between a and $a\sqrt{3}$. The most probable measurable size is:

$$d_0 = \frac{a(1+\sqrt{3})}{2} = 1.37a$$

A statistical analysis performed on the distribution of measured d_0 parameters provided a mean of 3.4 µm and standard deviation of 1.0 µm. Magnetite volume (a^3) can thus be calculated from the following formula:

$$V_{mgt} = \frac{8{d_0}^3}{\left(1+\sqrt{3}\right)^3}$$

From the volume of magnetite, the volume fraction occupied by magnetite within a given volume of sample can be retrieved from:

$$\frac{V_{mgt}}{\Omega} = n \cdot V_{mgt}$$

Where n represents the number density of magnetite, which is calculated as:

$$n = \frac{\Delta N}{S \Delta z}$$

Where ΔN is the number of countable magnetite inclusions within the volume of the observed matrix crystal; S is the section area of the matrix crystal (calculated with ImageJ); Δz is the thickness of the matrix crystal (corresponding to the thickness of the thin section: 80 μm). According to our estimates, n is comprised between 1.2×10^{-5} and 5.5×10^{-5} μm^{-3}. This procedure allowed us to estimate the volume fraction of magnetite varying between 0.0002 and 0.001.

Considering the above calculated volume fraction of magnetite, the volume of magnetite in sample Al9564 can be retrieved from its mass (117 mg), given a density of 3.2 g cm^{-3} for a harzburgite, obtaining a volume of 0.037 cm^3. Since olivine occupies about 70% of the total volume in our sample, the actual olivine volume to be considered is 0.026 cm^3. Given the volume fraction occupied by magnetite in a given volume of olivine, the volume of magnetite contained in 0.026 cm^3 of olivine is comprised between 0.4×10^{-5} and 3×10^{-5} cm^3. From magnetite density (5.2 g cm^{-3}) and magnetite molar mass (231.533 g mol^{-1}) the magnetite moles per gram of sample Al9564 result within the range 1-10 μmol g^{-1}. This range well contains the mass spectrometry estimate of H_2 amount of 6.2 μmol g^{-1}, supporting the equimolar relationship between H_2 and magnetite assumed in our chemical modelling.

4. Results

4.1. Mineral chemistry of host olivine, inclusion infillings and micro-Raman results

325 The major element compositions of the host olivine and of inclusions daughter minerals
326 are reported in Table 1. The relative point analyses are portrayed in Figure 3 along with X-ray
327 compositional maps of chlorite + magnetite inclusion and the Fe-Mg profile concentration of
328 host olivine close to the inclusion cavity wall.
329 Host olivines are forsteritic in composition with X_{Mg} [Mg/(Mg+Fe)] = 0.90 and are
330 homogeneous from core to rim (Table 1). An exception was made for very thin rims close to
331 some inclusions, showing a slight increase in Mg concentration (Figs. 3F and 4). These values
332 are comparable with those of spinifex olivine from literature (e.g., Padrón-Navarta et al. 2011).
333

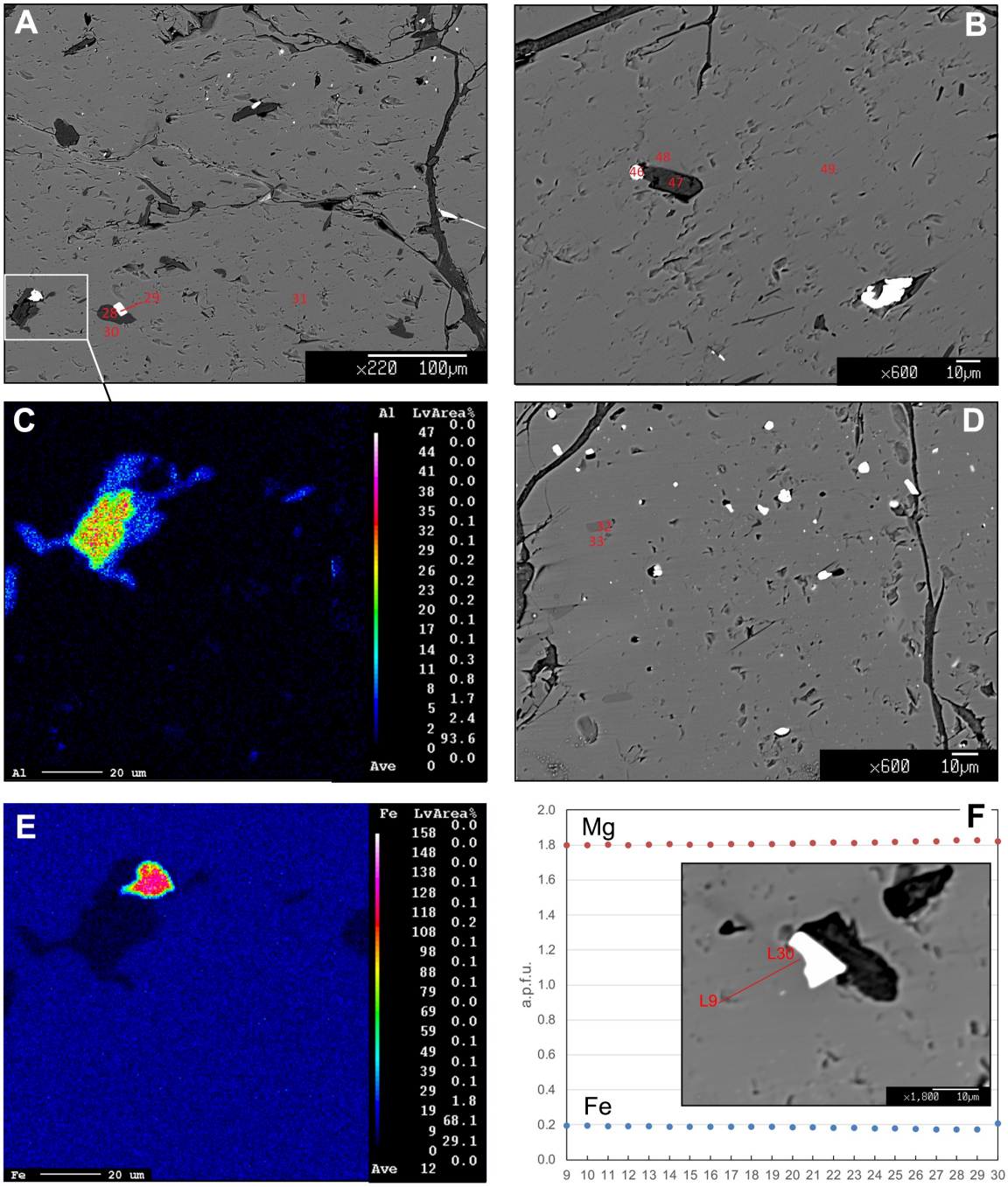

Figure 3: Backscattered electron microscope images (A,B,D and inset of F) of point analyses of some of the analysed inclusions and host olivine reported in Table 1. (C,E) X-ray Al and Fe maps of the inclusion within the white frame of (A), showing chlorite as daughter mineral in the magnetite-bearing inclusion. (F) Fe and Mg concentration profile along the line analysis shown in the inset, indicating a narrow slight zonation of olivine in correspondence of the inclusion interface.

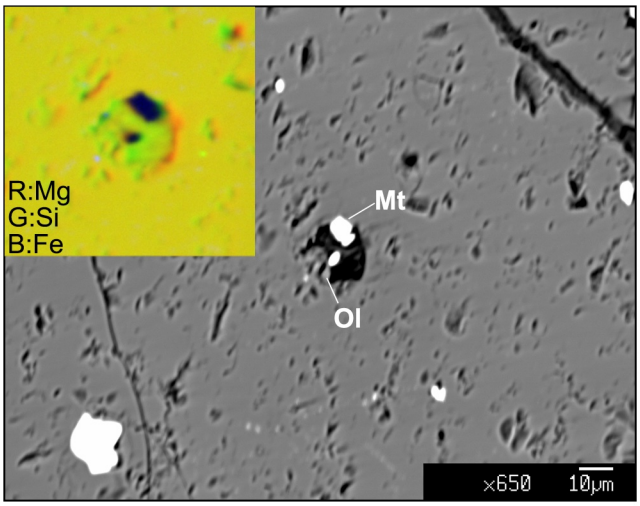

Figure 4: BSE image of a magnetite-bearing multiphase inclusion, containing a micron-size olivine intergrown with serpentine. The inset is the RGB combination of X-ray elemental map (Mg, Si, Fe) of the multiphase inclusion, showing a narrow Mg increase in olivine in correspondence of the cavity inclusion interface.

*Table 1: Oxide wt% and atoms per formula unit of host olivine and orthopyroxene, magnetite, chlorite and serpentinte in different inclusions. Olivine and magnetite are recalculated based on 3 cations; orthopyroxene on 4 cations; chlorite on 20 cations and 36 oxygens; serpentine on 116 oxygens. *=total iron as Fe^{2+}; **=Fe^{3+} calculated on stoichiometry; $Fe^{3+}/\Sigma Fe$ of olivine and magnetite from SMS analyses; n.a. = not analysed; b.d.l = below detection limit.*

Point analyses	7	28	29	30	31	32	33	46	47	48	49
Microstrutructural position	Ol host rim	Inc1-Serp	Inc1-Mgt	Inc1-Ol-wall	Ol host	Inc2-Opx	Inc2-Ol-wall	Inc7-Mgt	Inc7-Chl	Inc7_Ol-wall	Ol host
SiO_2	40.69	41.24	0.07	40.83	41.06	57.61	40.73	0.09	33.57	40.98	41.02
TiO_2	0.04	0.04	0.21	0.01	0.01	0.02	0.01	0.07	0.01	0.02	0.04
Al_2O_3	0.01	3.82	0.05	b.d.l.	0.02	0.07	b.d.l.	b.d.l.	13.75	b.d.l.	0.01
Cr_2O_3	b.d.l.	0.16	0.65	b.d.l.	b.d.l.	0.07	b.d.l.	0.33	0.61	b.d.l.	b.d.l.
FeO*	9.9	4.1	92.5	9.5	9.5	7.0	10.0	92.4	3.88	9.53	9.53
MgO	48.81	37.04	0.59	49.55	49.64	35.56	50.30	0.43	33.95	49.81	49.57
MnO	0.16	0.03	0.04	0.30	0.28	0.20	0.23	0.09	0.02	0.21	0.24
NiO	0.40	0.09	0.50	0.23	0.28	0.08	0.45	0.37	0.15	0.25	0.27
CaO	b.d.l.	b.d.l.	0.05	b.d.l.	0.01	0.09	0.02	b.d.l.	0.04	b.d.l.	b.d.l.
Na_2O	b.d.l.	b.d.l.	b.d.l.	0.01	b.d.l.	0.01	0.02	0.02	b.d.l.	0.01	b.d.l.
Sum	100.06	86.56	94.69	100.47	100.80	100.67	101.79	93.79	85.98	100.82	100.67
Si	1.00	32.27	0.00	0.99	1.00	1.97	0.98	0.00	6.43	0.99	1.00
Ti	0.00	0.02	0.01	0.00	0.00	0.00	0.00	0.00	0.00	0.00	0.00
Al	0.00	3.52	0.00	b.d.l.	0.00	0.00	b.d.l.	b.d.l.	3.10	b.d.l.	0.00
Cr	b.d.l.	0.10	0.02	b.d.l.	b.d.l.	0.00	b.d.l.	0.01	0.09	b.d.l.	b.d.l.
Fe^{3+}	0.00	0.00	**1.96	0.00	0.00	0.00	0.00	**1.98	0.00	0.00	0.00
Fe^{2+}	*0.20	*2.71	0.96	*0.19	*0.19	0.20	*0.20	0.96	*0.62	*0.19	*0.19
Mg	1.79	43.20	0.03	1.80	1.80	1.81	1.80	0.03	9.69	1.80	1.80
Mn	0.00	0.02	0.00	0.01	0.01	0.01	0.00	0.00	0.00	0.00	0.00
Ni	0.01	0.06	0.02	0.00	0.01	0.00	0.01	0.01	0.02	0.00	0.01
Ca	b.d.l.	b.d.l.	0.00	b.d.l.	0.00	0.00	0.00	b.d.l.	0.01	b.d.l.	b.d.l.
Na	b.d.l.	b.d.l.	b.d.l.	0.00	b.d.l.	0.00	0.00	0.00	b.d.l.	0.00	b.d.l.
Sum Cations	3.00	81.90	3.00	3.00	3.00	4.00	3.00	3.01	19.97	3.00	3.00
Sum Charges	8.00	232.00	7.99	7.99	8.00	11.95	7.96	3.00	56.00	7.99	8.00
X_{Mg}	0.90	0.94	0.03	0.90	0.90	0.90	0.90	0.03	0.94	0.90	0.90
$Fe^{3+}/\Sigma Fe$	0.09	n.a.	n.a.	0.00	0.00	n.a.	0.00	n.a.	n.a.	0.00	0.00

Regarding the inclusions mineral infillings, they correspond to magnetite, ±orthopyroxene and step-daughter minerals including chlorite, talc, and serpentine. The most abundant mineral is

magnetite, whose composition is almost stoichiometric and contains traces amounts of TiO_2, Cr_2O_3 and MgO (Table 1). Rare orthopyroxene inclusions are enstatite (X_{Mg} = 0.90). Chlorite minerals are Mg-rich and Al-poor, close to clinochlore composition (Table 1) and in agreement with the chlorite compositions from spinifex-like samples reported by Padrón-Navarta et al. (2011). Some chlorites show a slight zoning with decreasing Al from core to rim (Fig. 3C). Serpentine composition is variable and likely related to its occurrence as antigorite or chrysotile within the inclusion. Serpentine (antigorite) composition in Figures 1 and 3A shows a high Al content (Table 1), similar to that reported by Padrón-Navarta et al. (2013), and the Al/Si ratio falls along the Tschermak's exchange vector in the range of the maximum solubility of Al in antigorite at eclogite facies conditions (see Fig. 1 of Padrón-Navarta et al., 2013).

Detailed micro-Raman spectroscopy enabled to reconstruct the peak mineral assemblage in the inclusions and the step-daughter minerals formed after the interaction between water and olivine upon exhumation and inclusions cooling. Among the early-stage minerals, olivine, orthopyroxene and probably chlorite coexisted with magnetite and water (Figs. 3 and 4). As shown in Figure 5A, some of the multiphase inclusions containing magnetite (inset 1 of Fig. 5A; see Shebanova and Lazor, 2003 for reference spectrum) show half of their volume filled by talc, identified by the OH vibration near 3677 cm^{-1} (inset 2 of Fig. 5A) and its most intense Raman band at 678 cm^{-1}, and minor bands near 112, 195, 364, 433 cm^{-1} (Fumagalli et al., 2001). Part of the cavity wall and the remaining space of the inclusions is over/inter-grown with micro- to nanocrystals of chrysotile + brucite as reported in the Raman spectrum of Figure 5A (inset 3). The low and high frequency regions are dominated by chrysotile and olivine Raman bands, whereas in the OH region is visible the most intense brucite Raman band with a well-defined peak near to 3650 cm^{-1} (see the peak with the asterisk in the inset 3 of Fig. 5A).

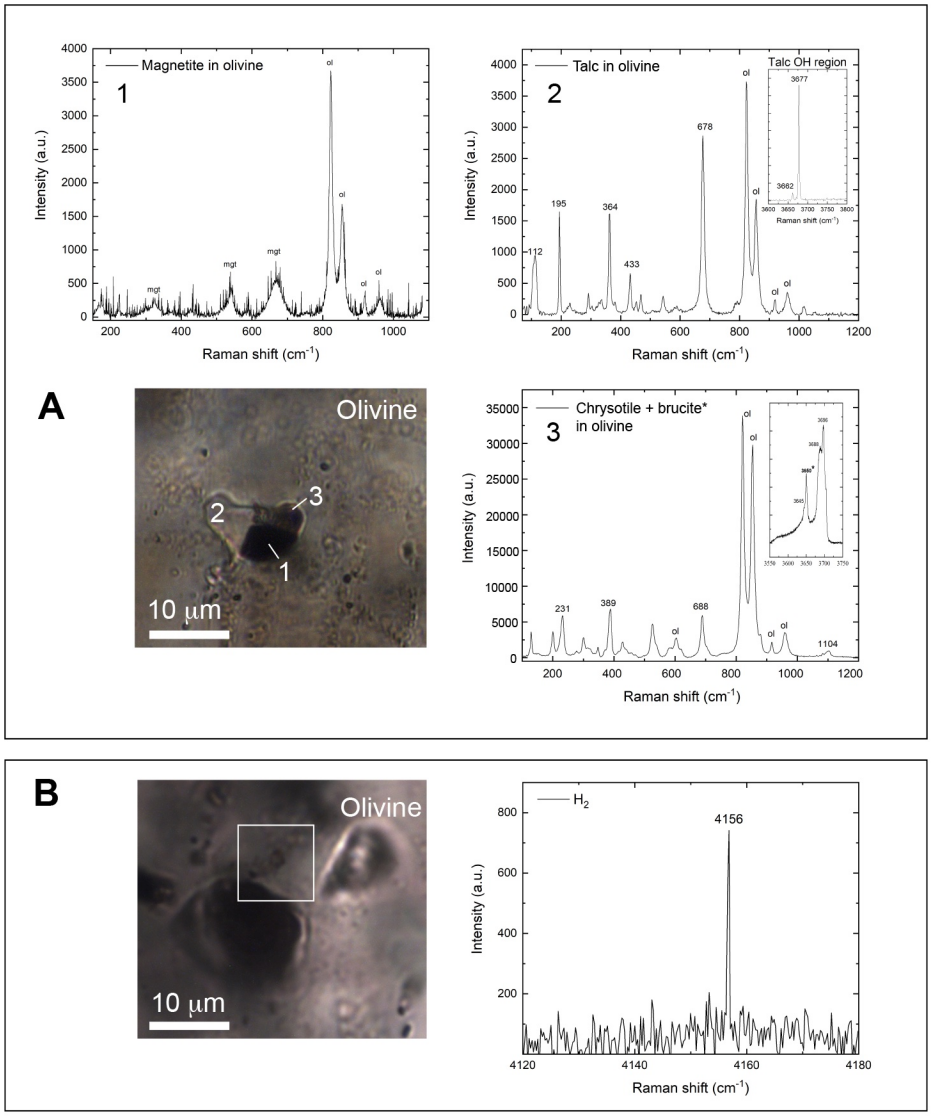

Figure 5: (A) Optical micrograph of multiphase inclusion in olivine and representative Raman spectra of its mineral infillings. For talc and chrysotile + brucite the O-H stretching modes in the range between 3600 and 3800 cm-1 wavenumbers are also reported. Spectra are baseline corrected. (B) Optical micrograph of multiphase inclusion in olivine and hypothetical H_2 peak retrieved from a 9×8 points grid map (white frame) in the host olivine close to the inclusion wall.

The detected serpentine polymorph is ascribed to chrysotile according to the most intense and characteristics Raman bands near 231, 389, 688 and 1104 cm^{-1} (e.g., Petriglieri et al. 2015 and Rooney et al. 2018). Interestingly, a weak vibration at 4156 cm^{-1} has been identified as probable H_2 in a grid map performed in the olivine host, close to the inclusion wall (Fig. 5B).

4.2. Bulk inclusions and olivine H_2O - H_2 measurements

To document the presence of molecular hydrogen in olivine we performed quantitative QMS analyses (see details of the method in section 3.3) of the fluid phase trapped in the multiphase inclusions and of the olivine crystals hosting the inclusions.

Table 2: Quantitative analysis of the fluid liberated from hand-picked olivine (1.00 g) after fine grinding. b.d.l= below detection limit.

sample	H_2O (µmol)	2σ	H_2 (µmol)	2σ	CO_2 (µmol)	2σ	CH_4 (µmol)	2σ
AL95_64	104.4	0.6	6.2	0.1	1.7	0.4	b.d.l.	-
blank control	2.30	0.04	b.d.l.	-	b.d.l.	-	b.d.l.	-

As shown in Table 2, 1.00 g of olivine contains 104 ± 1 µmol of H_2O, 6.2 ± 0.1 µmol of H_2 and very low contents of CO_2 close to the detection limit. H_2 is well above the detection limit (close to 1 µmol) and it has not been found in blank control (Table 2). Note that water or CO_2 do not derive from hydrous/carbonate phases occurring as inclusions or filling microfractures because the measurements were performed at low temperature (~90 °C). If free water is the residual fluid still preserved in the multiphase inclusions (Scambelluri et al., 2001), molecular hydrogen can occur only trapped in the olivine lattice or as nanoscale single inclusions outside the multiphase inclusions (see section 5.2 of the discussion). This assumption is confirmed by the micro-Raman analyses of dozens of inclusions that never revealed H_2 within the inclusions and by the occurrence of weak vibrations only in the olivine close to the inclusion's walls (Fig. 5B).

4.3. $Fe^{3+}/\Sigma Fe$ of olivine

SMS analyses have been carried out in 6 olivine hosts among two rock sections (AL9564b1 and AL9564b2). A total of 22 spectra on magnetite inclusions and 6 spectra on solely the olivine hosts have been acquired. Our data on magnetites in terms of chemical compositions and magnetic properties have been deeply investigated by Campione et al. (2022).

In this work we concentrate on olivine spectra collected far from magnetite inclusions, which show the presence of some ferric iron ($Fe^{3+}/\Sigma Fe$ = 0.05 to 0.08; Table 1), while for those acquired near to inclusion clusters only Fe^{2+} has been detected (Fig. 6A). The absence of Fe^{3+} in the olivine structure near to magnetite inclusions is consistent with the deduced mechanism of inclusion formation (see section 5.2 and Campione et al. 2020).

The olivine signal in SMS spectra is present also when magnetite crystals are analysed because they occur as inclusions embedded inside the olivine. Among these spectra collected directly at the magnetite inclusions, the olivine signal sometimes displays an additional doublet related to Fe^{3+} with values up to 24 % of the total measured iron content (Fig. 6B).

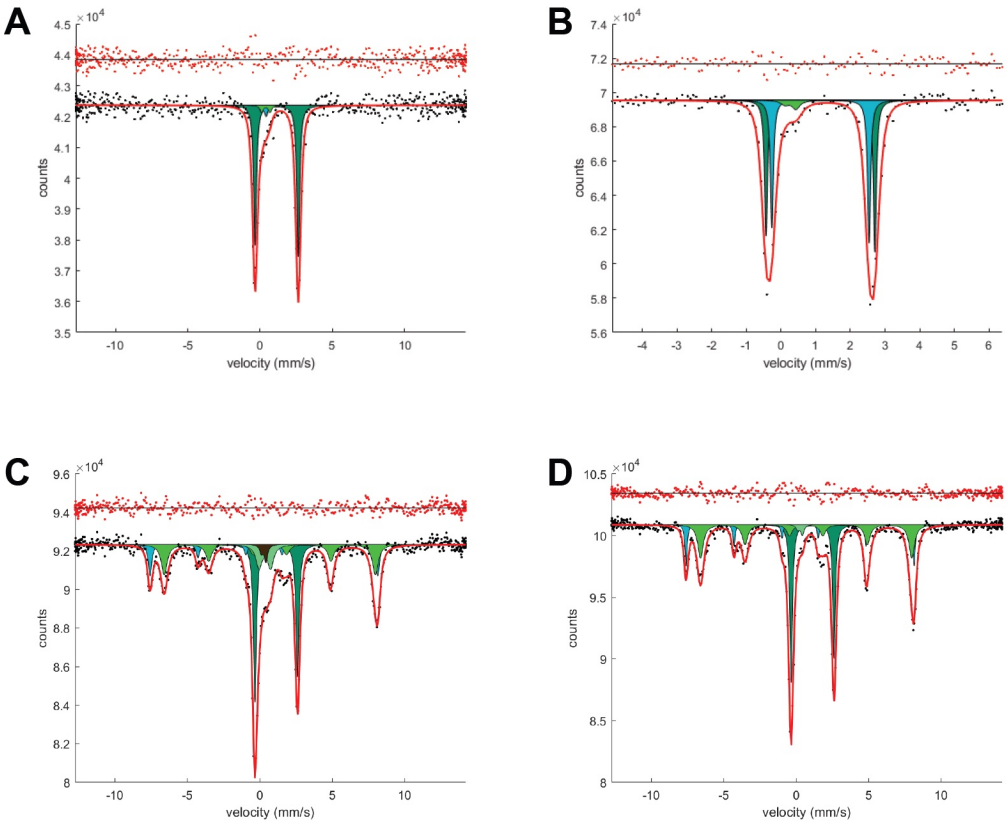

Figure 6: (A, B) Two SMS spectra of olivine hosts displaying variation in ferric iron as a function of their proximity to magnetite inclusions (left spectrum collected far from inclusions and right spectrum collected near to a magnetite inclusion). The ferric iron content is present in the spectrum on the left (A) as a doublet in light green colour, while the peak arising in the middle of the Fe^{3+} doublet is related to the Be lenses contribution. The same contribution from Be lenses is present on the right-hand spectrum (B) in light green colour, while no Fe^{3+} has been detected. Note that the two spectra, A and B, were collected using different velocity scales (±12 mm s^{-1} in A and ±5 mm s^{-1} in B). As a consequence, in (B) it was possible to distinguish and fit the two olivine metal sites (two doublets), M1 and M2, whereas in (A), and (C, D), only one doublet was used due to the lower velocity resolution and presence of several other components, i.e., from magnetite. (C, D) SMS spectra of two magnetite inclusions within the same olivine host and located about 500 µm apart one from another. (C) SMS spectrum of magnetite inclusions and their olivine host showing an intense Fe^{3+} doublet in light green colour and related to the olivine structure, in black is reported the contribution from the Be lenses. (D) SMS spectrum without the presence of Fe^{3+} in the olivine structure, the light green doublet is the contribution from the Be lenses.

These values clearly cannot be attributed solely to the incorporation of Fe^{3+} in olivine, which is unrealistic, instead could be addressed to chromite exsolved lamellae, which are considered to be part of secondary exsolution products during exhumation processes and possibly to the exposition to large temperature swings (Ruiz Cruz et al., 1999). Fe^{3+} content in chromite lamellae is significant and can be detected in the spectra as a minor doublet component, with center shift values of ~0.3 mm s^{-1}, which represent the convolution of Fe^{3+} in olivine and chromite, with hyperfine parameters expected for Fe^{3+} in octahedral coordination (Osborne et al., 1981). The weak Fe^{2+} chromite signal cannot be resolved from the measured spectra either because it is too low to emerge from the background noise level (lower than ~2 % of the total signal), either because its low intensity is masked by the predominant Fe^{2+} and Fe^{3+} components of olivine and chromite respectively, e.g., Figure 6C. Moreover, note that the large velocity scale used in this study, ±12 mm s^{-1}, was necessary to resolve the magnetic sextet of the magnetite inclusions, at the expenses however of the velocity resolution, diminishing the possibility to clearly distinguish low intensity components.

5. Discussion

The studied inclusions are microsystems showing the chemical behaviour of a fluid produced by slab de-serpentinization during its interaction with olivine in a closed system at pressure and temperature typical of subduction conditions. As discussed by Scambelluri et al. (2001), the fluid trapped by metamorphic olivines of spinifex-like harzburgites from Almirez is water rich but also contains some silica, aluminium, and fluid mobile elements, typical of the compositions of slab-derived fluids. As demonstrated by experimental works (Tropper and Manning, 2007; Manning et al., 2010) and modelled in Campione et al. (2017), aluminium

462 solubility in subduction fluids (even in pure water) at high pressure may be significant. The
463 occurrence of Al-bearing phases in the studied multiphase inclusions (chlorite) likely derive
464 from the initial interaction between the host olivine and an Al_2O_3-rich fluid. The early
465 precipitation of chlorite consumed the pristine Al_2O_3 of the fluid, living room to the subsequent
466 interaction with an almost pure residual water. The chemical exchange between inclusion fluid
467 and olivine therefore started soon after the entrapment, at peak *P-T* conditions of 1.6-1.9 GPa
468 and 650-700 °C, and continued during cooling along the retrograde path, as reconstructed from
469 the stability fields of the step-daughter minerals assemblage. Because the interaction of olivine
470 with the fluid actually occurred with almost pure water, and because the possible addition of Al
471 in the system stabilises chlorite without changing the position of the other mineral assemblages,
472 for the sake of simplicity we decided to show the possible reaction sequence during post-
473 entrapment interaction in a simple MSFH(O) phase diagram, as shown in Figure 7.

474 The sequence (in addition to chlorite) indicates the coexistence of olivine with (1)
475 orthopyroxene, (2) talc, (3) antigorite and (4) the destabilisation of olivine and antigorite into
476 brucite and low-temperature chrysotile serpentine, as recognised by Raman analyses (Fig. 5A).
477 Magnetite is always stable. The fact that magnetite is not a product of retrograde
478 serpentinization of the olivine host but is a primary product of the redox reaction between
479 inclusion fluid and the olivine is proven by the documented epitaxy of olivine and magnetite
480 and by the observed volume proportions of magnetite crystals in each inclusion (Figs. 1, 4 and
481 5) (Campione et al., 2020). The observed magnetite proportions are much higher than those
482 obtained during experimental hydration of olivine (Lamadrid et al., 2017). This observation
483 further supports the crystallisation of magnetite as a result of a kinetic-controlled reaction rather
484 than a formation under thermodynamic equilibrium conditions as those reached during
485 experiments. Campione et al. (2020) in fact demonstrated that the evolution of the fluid/olivine

interaction is controlled by the process of magnetite crystallisation along with the energetic cost related to the nucleation and growth of the product phases.

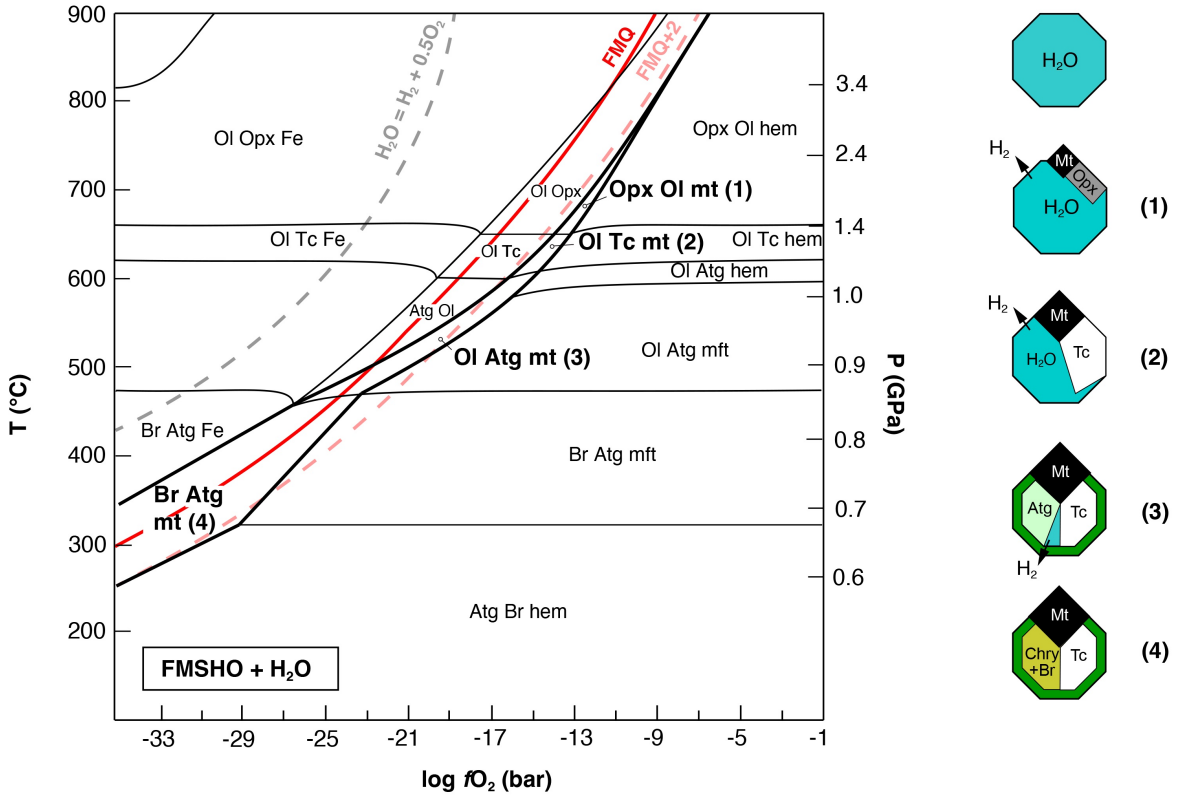

Figure 7: Thermodynamic model of the system Si-Mg-Fe-O_2-H_2O calculated along a retrograde P-T path based on the mineral assemblages formed from the retrograde reaction between the residual water in the multiphase inclusions and the olivine host. This path is roughly consistent with that described by Laborda-López et al. (2018). Ol, Opx, Tc, Atg, Br correspond to olivine, orthopyroxene, talc, antigorite and brucite solution models as described in Section 3.5. Fe, hem, mt, mft correspond to pure iron, hematite, magnetite and magnesioferrite. The Fayalite-Magnetite-Quartz buffer (red curve) and the water buffer (dashed grey curve) are reported for reference. On the right side of the figure, the reconstructed sequence of the mineral assemblages within the inclusions is reported. The green rim in the inclusion represents the forsterite rich layer formed after water/olivine interaction (Fig. 3). H_2 starts to diffuse in the olivine host as soon as magnetite nucleates (Step 1), ending when the reaction stops (Step 4). See text for details on the redox reactions.

A recent work by Zelenski et al. (2022) shows that fluid-spinel inclusions in magmatic olivine from Tolbachik (Kamchatka) have textural relations almost identical to those of multiphase inclusions of this work. They interpret the spinel formation as the result of a redox reaction between water and olivine forming a new olivine with forsterite content up to 96-99% and SiO_2 that dissolves in the fluid coupled with production of H_2. We will discuss in the next sections how this process can be triggered by the energy gain related to the nucleation of epitaxial magnetite.

506

507 *5.1. The synergistic role of epitactic magnetite and H_2-permeable olivine host*

508

509 The phase diagram reported in Figure 7 attempts to reproduce the oxygen fugacity
510 conditions of the host olivine and water system, starting from peak conditions where
511 orthopyroxene is stable, along a retrograde path based on the retrograde reactions between the
512 residual water and olivine that stabilises talc, antigorite and then serpentine + brucite. The
513 inclusions assemblages 1 to 3 record oxygen fugacitites of FMQ+2 (dashed light red curve),
514 whereas assemblage 4 ranges from FMQ-2 to FMQ+2, that are far from the redox conditions
515 of the buffer of water, where H_2 can be stable (left side of the dashed grey curve). These
516 modelled oxygen fugacities are perfectly consistent with the redox conditions measured by the
517 experimental works of Iacovino et al. (2020) and Maurice et al. (2020) during (and after)
518 dehydration of antigorite at subduction conditions.

519 Hydrogen production is usually attributed to serpentinization (e.g., Klein et al., 2013),
520 which can be viewed as the development of two parallel reactions:
521 oxidation of the fayalite component of olivine

522 $3\ Fe_2SiO_4$ [fayalite] + $H_2O \rightarrow Fe_3O_4$ [magnetite] + $3\ FeSiO_3$ [ferrosilite] + H_2 (3)

523 and hydration of olivine

524 $(Mg,Fe)_2SiO_4$ [olivine] + $(Mg,Fe)SiO_3$ [orthopyroxene] + $2\ H_2O \rightarrow (Mg,Fe)_3Si_2O_5(OH)_4$
525 [serpentine] (4)

526 bringing to the overall reaction:

527 $6\ (Mg,Fe)_2SiO_4$ [olivine] + $7\ H_2O \rightarrow Fe_3O_4$ [magnetite] $+ 3\ (Mg,Fe)_3Si_2O_5(OH)_4$ [serpentine]
528 $+ H_2$ (5)

529 Under the conditions of antigorite breakdown at high pressure, reaction (4) is suppressed, and
530 reaction (3) fully describes the chemical processes in progress within the inclusions, whereas,

along the retrograde path, the fayalite component of olivine is still oxidised by reduction of the trapped residual water following the serpentinization reaction (5). As shown in Figure 7, all the above reactions occur at decreasing oxygen fugacity, from FMQ+2 to FMQ, but high enough to stabilise magnetite from its nucleation at the peak to its continuous growing during the fluid/olivine interaction.

Pure water trapped in olivine inclusions at high pressure may trigger the redox reaction (3), aided by two factors: (i) the magnetite forms an epitaxial interface with olivine (Fig. 1) and (ii) molecular hydrogen can abandon the inclusion cavity by diffusion through the olivine host (Fig. 5B; Table 2). Note that point (i), as discussed before, does not occur in the case of the direct serpentinization reaction between trapped fluid and olivine host during retrogression because the hydration of olivine hinders the possibility of developing an epitaxial interface between its surface and magnetite (see Lamadrid et al., 2017). This implies that the fluid entrapment and its reaction with olivine at peak conditions were outside the stability field of serpentine (i.e., antigorite) and that the epitaxial growth of magnetite, yielding oxidation of the fayalite component of host olivine, ruled the progressive fluid/olivine thermodynamic equilibria.

From all the reactions involving oxidation, it is apparent that the developed hydrogen is equimolar with magnetite. In our samples, this condition is evident from the consistency between the mass spectroscopy determination of hydrogen content and the optical micrograph-based determination of the volume fraction of magnetite (Table 2; section 3.6 and Fig. 2).

Another characteristic of these reactions is the enrichment in silica of the cavity volume resulting from the oxidation reaction, as also shown in the experimental results of Zelenski et al. (2022). This must be compensated by the precipitation of a phase with a higher silica fraction with respect to olivine (e.g., orthopyroxene, as assumed in reaction 3). Evidence of the silica enrichment is given by the occurrence of single orthopyroxene inclusions (Fig. 3) and talc in

556 the multiphase inclusions (Fig. 5A) likely formed after hydration of a previous orthopyroxene
557 reacting with residual water (Fig. 7).

558 The hypothesis of magnetite and orthopyroxene coprecipitation (reaction 3) allows to
559 virtually preserve the total volume occupancy of the product phases after the reaction. Indeed,
560 for each mole of reacted olivine (molar volume: 45 $cm^3\ mol^{-1}$), one-third mole of water is
561 consumed (molar volume at 4 GPa and 800 °C: 14 $cm^3\ mol^{-1}$) and one-third mole of magnetite
562 (molar volume: 45 $cm^3\ mol^{-1}$) and one mole of orthopyroxene (molar volume: 32 $cm^3\ mol^{-1}$) are
563 produced. However, the evidence of a constant volume fraction among inclusion phases (e.g.,
564 magnetite/water, as resulting from the mass spectroscopy analyses reported in Table 2) points
565 to an equilibrium reached by the inclusion system which is likely governed by volume
566 variations occurring as an effect of the reaction progress, which in turn determine a progressive
567 pressure increment or decrement within the closed system of the inclusion. Following reaction
568 (2), the reacted water is equimolar to magnetite, and then the molar content of remnant water is
569 expected to be a factor of 17 higher than that of magnetite (and molecular hydrogen) in every
570 inclusion (Table 2).

571 Based on reaction (3) and mass spectrometry data of Table 2 referring to a rock sample
572 of 1.00 g, the following equivalences hold:

573 6.2 μmol H_2 ≡ 6.2 μmol Mgt ≡ 19 μmol Fa ≡ 190 μmol Fo_{90} ≡ 38 μmol Fe^{2+}

574 The production of 6.2 μmol of magnetite (Mgt) requires the dissolution of 19 μmol of fayalite
575 (Fa) or 190 μmol of 90 mol% of forsterititic olivine (Fo_{90}), which provide 38 μmol of Fe^{2+}. In
576 volume terms, the production of 0.28 mm^3 of magnetite requires the dissolution of 0.87 mm^3 of
577 fayalite or 8.4 mm^3 of Fo_{90}. The total moles of water required to dissolve this volume of olivine
578 is 104.4 μmol + 6.2 μmol = 110.6 μmol, corresponding to a volume of 1.5 mm^3. By considering
579 these amounts as pertinent to a single inclusion, the available cavity volume is that
580 corresponding to the initial amount of water (1.5 mm^3). This corresponds to the volume of a

spherical cavity of radius 0.72 mm. This cavity volume must be compared with the required Fo_{90} volume: 8.4 mm^3. This volume is enclosed in a circular crown of the surrounding olivine of thickness 0.61 mm. Hence, the thickness of the surrounding olivine volume providing all the Fe for magnetite is of the order of the cavity radius. Then, if we assume a negligible role of the migration of Fe towards the inclusion, a magnetite inclusion forms thanks to the dissolution of a volume of Fo_{90} which is 30 times larger than that of magnetite and almost 6 times larger than that of the available water. It is likely that iron is not provided only by a dissolution-reprecipitation mechanism but also by its migration from the whole olivine matrix to the inclusion cavity likely favoured by an exchange with Mg from the inclusion to olivine. If we admit the migration of the required Fe from the surrounding olivine matrix without excess olivine dissolution, as modelled by Zelenski et al., (2022), this would bring to a 6% decrement of Fe content, with a change from Fo_{90} to barely Fo_{91}:

1.0 g Fo_{90} ≡ 6.8 mmol Fo_{90} ≡ 680 µmol Fe^{2+} ≡ 6120 µmol Mg^{2+}

In conclusion, magnetite is grown thanks to the occurrence of the migration of Fe^{2+} from the olivine matrix to the inclusion cavity along with a dissolution-reprecipitation process. Note that the excess olivine is re-precipitated in the form of a thin forsterite-rich layer, as shown in Figure 2.

Pure water trapped in inclusions in metamorphic olivine may trigger the oxidation of the fayalite component of olivine, producing a mineral assemblage made of magnetite and orthopyroxene and producing hydrogen, where the redox couples are Fe^{2+} of olivine (oxidized to Fe^{3+}) and H^+ of H_2O (reduced to H_2). The driving force of the whole process is the building up of an epitaxial interface between olivine and magnetite that helps reducing the activation barrier for the magnetite nucleation. During this process, epitaxial match has a strong impact on the kinetics through phenomena that involve surfaces and interfaces between phases of finite size. A favourable epitaxial match therefore allows to increase the nucleation rate of magnetite

606 which, under different conditions, might be so low to prevent the observability of magnetite
607 crystallites.
608
609 *5.2. Olivine oxidation and hydrogen production*
610
611 As shown in Figure 1A and described by Scambelluri et al. (2001), magnetite-bearing
612 multiphase inclusions occur concentrated in core clusters in olivine that shows clear rims.
613 Mossbauer analyses reveal that olivines are zoned in Fe^{3+}, with Fe^{3+}-free cores containing the
614 inclusions and rims that have up to 9% of $Fe^{3+}/\Sigma Fe$ (Fig. 6 and Table 1). This zonation may
615 result from iron diffusion from core to rim as described in the experimental results of Mackwell
616 (1992). On the other hand, if we consider the olivine oxidation process described in the previous
617 sections, it is more likely that the olivine rim represents a new crystallisation stage in absence
618 of free water at oxidised conditions. Note that our samples do not contain any sulphide phases
619 nor in the inclusions, neither in the mineral assemblage.
620 The phase relations of olivine-water system at peak conditions and variable fO_2 and fH_2
621 conditions are reported in Figure 8, where the blue line represents an aqueous fluid with water
622 activity ~ 1 in the O-H system. At fluid-present conditions, moving on the blue fluid curve, the
623 dissociation of water ($H_2O = H_2 + 0.5\ O_2$) requires that at fixed fO_2, fH_2 becomes a dependent
624 variable and vice versa. In the presence of water, the peak association olivine + orthopyroxene
625 + magnetite at the beginning of the fluid/olivine interaction (nucleation of magnetite) is stable
626 at FMQ+2 (Fig. 7 and 8), indicating a relatively oxidised condition. This hypothesis should be
627 regarded as a proof by contradiction, because it is very unlikely that an external (fluid) agent is
628 capable to modify the fO_2 or fH_2 as needed, unless other components (such as carbon or sulfur)
629 are involved as fluid species lowering the water activity. However, if the inclusions are
630 impermeable to H_2O but not to H_2, although the chemical potential of oxygen (and therefore

that of fH_2) is kept constant inside the inclusion, the hydrogen diffusion in the olivine host shifts the equilibrium (3) in the direction of the products, following the Le Chatelier's principle, promoting the continuous growth of magnetite and the formation of molecular H_2 in the olivine host, where the fH_2 of olivine tends to increase to very high values.

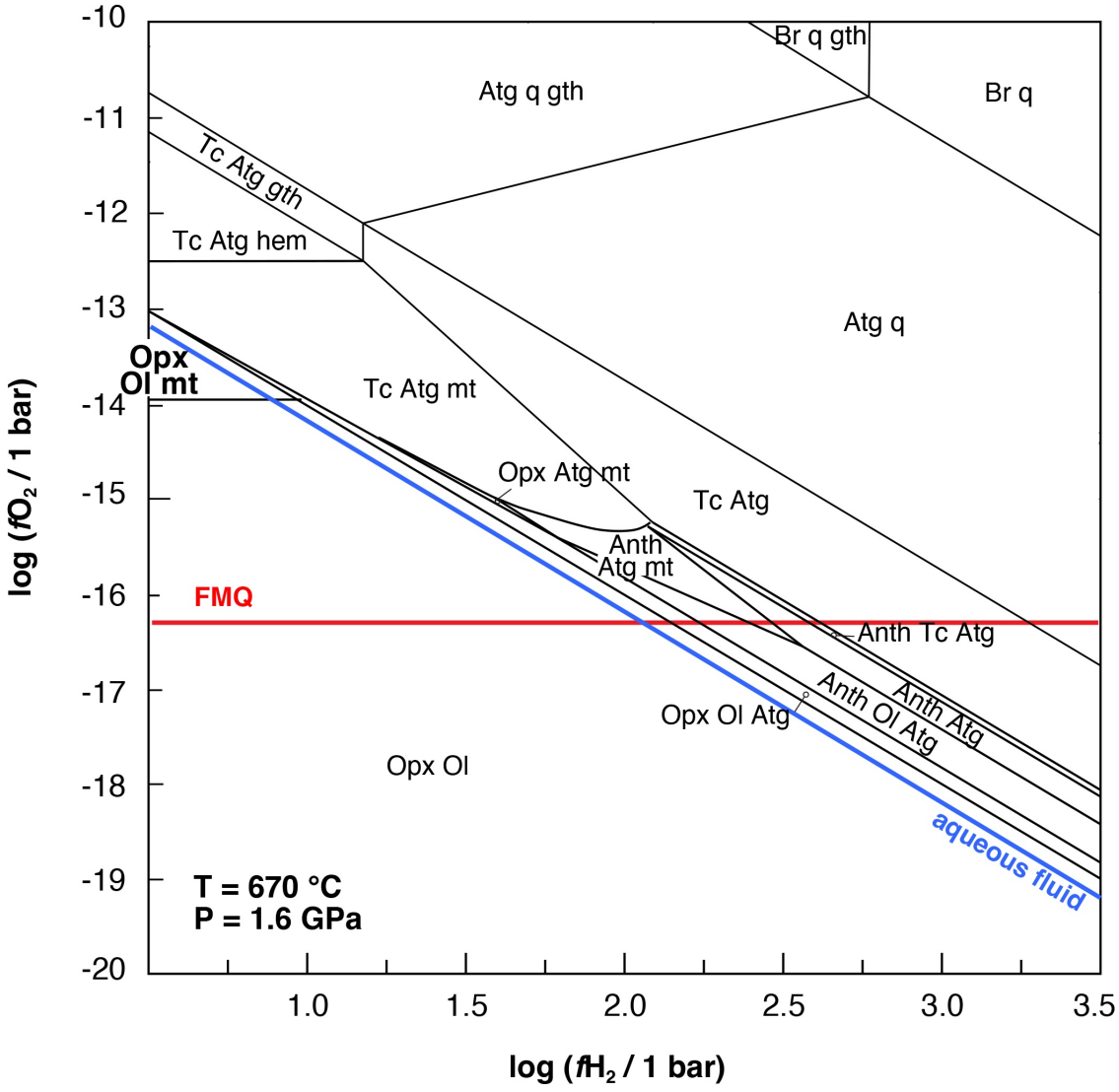

Figure 8: Phase stabilities under variable fO_2 and fH_2 condizione in the same system as Figure 7 calculated at peak conditions of Bretscher et al. (2018) at 1.6 GPa and 670 °C. The red line corresponds to the log fO_2 value of Fayalite-Magnetite-Quartz buffer, while the blue line is the aqueous fluid.

Conversely, an accumulation of H_2 inside the inclusion would hinder the reaction progress, because high fH_2 values are not allowed in equilibrium with water and magnetite. It is worth of note that reaction (3) allows molecular H_2 formation in the olivine host at fO_2 far more oxidizing than those required to dissociate H_2O to H_2 (Fig. 7). Indeed, at the P–T–fO_2–fH_2 conditions of

644 our assemblage the molar fraction of molecular H_2 in the aqueous fluid should be negligible
645 (0.15×10^{-5}), meaning that reaction (2) cannot produce in the inclusions the amount of hydrogen
646 measured in our bulk samples, unless hydrogen diffusion in host olivine is considered. The
647 measured H_2/H_2O ratio is about 6% (Table 2), 5 orders of magnitude higher than that
648 corresponding to spontaneous water dissociation (see also Frost and Ballhaus, 1998; Evans and
649 Frost, 2021). Our conclusion is supported by the ability of silicates to store molecular hydrogen
650 at high pressures, as documented by the materials science literature (Schmidt et al., 1998;
651 Oyama et al., 2004; Efimchenko et al., 2012) and by Moine et al. (2020) in eclogites
652 equilibrated at 2.1–4.1 GPa and 805–1140°C. We infer that a similar behaviour is adopted by
653 olivine already at 1.6 GPa and 670°C, characterising the peak metamorphism in Almirez.
654
655
656 **6. Conclusions and perspectives**
657
658 Magnetite-bearing multiphase inclusions hosted by olivine are very common and occur
659 in different geodynamic scenarios. Some examples of these kind of occurrences in both fluid
660 and solid multiphase inclusions in subducted serpentinites have been described in olivine-
661 bearing veins derived by high-pressure deserpentinization in the Erro-Tobbio massif (Ligurian
662 Western Alps, Italy; Scambelluri et al., 1997) and in olivine from eclogite-facies garnet
663 metaperidotite and chlorite harzburgite bodies from Cima di Gagnone (Scambelluri et al, 2015).
664 Other important occurrences, in mantle domains far from subduction zones, have been reported
665 in olivines from intraplate metasomatised mantle from La Gomera and El Hierro (Canary
666 Islands) by Frezzotti et al. (1994) and Oglialoro et al. (2017), as well as from magmatic olivine
667 from Tolbachik (Kamchatka) by Zelensky et al. 2022. Furthermore, many occurrences of
668 topotaxial magnetite needles and tablets in mantle olivine have been described in mantle wedge

669 garnet peridotites from Sulu Belt, China (Malaspina et al., 2009b), interpreted as
670 dehydrogenation-oxidation processes (Hwang et al., 2008), and in xenolith samples from
671 different geodynamic scenarios (Ferré et al., 2013). In all these occurrences the presence of
672 molecular hydrogen in olivine was not analysed or investigated even if the role of water/olivine
673 interaction during mantle metasomatism may have triggered olivine's fayalite component
674 oxidation. The water/olivine interaction of our inclusions in meta-harzburgites from Almirez is
675 governed by the kinetic control of magnetite-olivine epitaxy. The olivine + H_2O system of these
676 natural microreactors simulates a process of oxidation of the mantle olivine by water, with
677 production of H_2 under oxidising conditions driven by epitactic magnetite. In these systems
678 pure water can be an effective oxidising agent, where oxygen is present in the form of magnetite
679 and H_2 can be produced at fO_2 conditions at which water cannot be dissociated (Fig. 5). The
680 occurrence of molecular hydrogen at oxidising conditions can be possible thanks to the olivine
681 ability to act as a trap for H_2 at high pressure.
682
683 **CRediT author statement**
684
685 **Nadia Malaspina:** Conceptualization, Methodology, Writing - Original Draft, Writing -
686 Review & Editing, Visualization, Funding acquisition. **Marcello Campione:** Methodology,
687 Validation, Investigation, Writing - Review & Editing. **Simone Tumiati:** Methodology,
688 Validation, Investigation, Writing - Review & Editing. **Mara Murri:** Visualization,
689 Investigation, Writing - Review & Editing. **Patrizia Fumagalli:** Investigation, Data curation,
690 Writing - Review & Editing. **Valerio Cerantola:** Investigation, Data curation, Writing -
691 Review & Editing. **Mattia La Fortezza:** Investigation. **Marco Scambelluri:** Supervision,
692 Resources, Writing - Review & Editing, Funding acquisition.
693

Declaration of Competing Interest

The authors declare that they have no known competing financial interests or personal relationships that could have appeared to influence the work reported in this paper.

Acknowledgments

N. Campomenosi (University of Hamburg) and A. Risplendente (University of Milano) are ackowledged for the analytical assistance in micro-Raman spectroscopy and electron microprobe respectively. We thank D. Bessas, A. Rosenthal and A. Chumakov for technical assistance during the beamtime at ID18 of ERSF. N. Malaspina also thanks J. Hermann and T. Pettke for constructive discussion. The manuscript benefited from detailed and critical comments by two anonymous reviewers.

Fundings

This work has been financed by the Italian Ministry of Education, University and Research (MIUR) PRIN 2017 - Prot. 2017ZE49E7_005 - The Dynamic Mass Transfer from Slabs to Arcs - Dynastars and MIUR-DAAD Joint Mobility Program (2018-NAZ-0023) - The redox state of the Earth's mantle: from the slab-mantle interface to the sub-continental lithosphere. N. Malaspina also acknowledges the University of Milano-Bicocca 2022-ATEQC-0015 "Redox processes and implications on C-O-H-S budget from the shallow crust to the deep mantle".

References cited

1. Brandon, A.D., Draper, D.S., 1996. Constraints on the origin of the oxidation state of mantle overlying subduction zones: an example from Simcoe, Washington, USA. Geochim. Cosmochim. Acta, 60(10), 1739-1749.
2. Bretscher, A., Hermann, J., Pettke, T., 2018. The influence of oceanic oxidation on serpentinite dehydration during subduction. Earth Planet. Sci. Lett., 499, 173-184.
3. Campione, M., La Fortezza, M., Alvaro, M., Scambelluri, M., Malaspina, N., 2020. Commensurate growth of magnetite microinclusions in olivine under mantle conditions. ACS Earth Space Chem., 4(6), 825-830.
4. Campione. M., Murri, M., Cerantola, V., Bessas, D., Rosenthal, A., Chumakov, A., Scambelluri, M., Malaspina, N. (2022) Magnetic ordering of magnetite inclusions in olivine at mantle depths in subduction zones. ACS Earth Space Chem., 6, 2755-2759.
5. Campione, M., Tumiati, S., Malaspina, N., 2017. Primary spinel + chlorite inclusions in mantle garnet formed at ultrahigh-pressure. Geochem. Persp. Lett., 4, 19-23.
6. Cannaò, E., Malaspina, N., 2018. From oceanic to continental subduction: Implications for the geochemical and redox evolution of the supra-subduction mantle. Geosphere, 14(6), 2311-2336.
7. Connolly, J.A., 2005. Computation of phase equilibria by linear programming: a tool for geodynamic modeling and its application to subduction zone decarbonation. Earth Planet. Sci. Lett., 236, 524-541.
8. Cottrell, E., Birner, S.K., Brounce, M., Davis, F.A., Waters, L.E., Kelley, K.A., 2021. Oxygen fugacity across tectonic settings. Magma redox geochemistry, Geophysical Monograph Series, 33-61.

9. Debret, B., Andreani, M., Muñoz, M., Bolfan-Casanova, N., Carlut, J., Nicollet, C., Schwartz S., Trcera, N., 2014. Evolution of Fe redox state in serpentine during subduction. Earth Planet. Sci. Lett., 400, 206-218.
10. Debret, B., Sverjensky, D.A., 2017. Highly oxidising fluids generated during serpentinite breakdown in subduction zones. Sci. Reports, 7, 1-6.
11. Duan, W. Y., Li, X. P., Schertl, H. P., Willner, A. P., 2022. COHS fluids released by oceanic serpentinite in subduction zones: Implications for arc-magma oxidation. Earth Planet. Sci. Lett., 594, 117709.
12. Efimchenko, V.S., Fedotov, V.K., Kuzovnikov, M.A., Zhuravlev, A.S., Bulychev, B.M., 2013. Hydrogen solubility in amorphous silica at pressures up to 75 kbar. J. Phys. Chem. B, 117, 422-425.
13. Evans, K.A., 2012. The redox budget of subduction zones. Earth Sci. Rev. 113, 11-32.
14. Evans, K.A., Elburg, M.A., Kamenetsky, V.S. (2012). Oxidation state of subarc mantle. Geology, 40(9), 783-786.
15. Evans, K. A., & Frost, B. R., 2020. Deserpentinization in subduction zones as a source of oxidation in arcs: A reality check. J. Petrol., 62(1), 1-32
16. Evans, K.A., Tomkins, A.G., 2020. Metamorphic fluids in orogenic settings. Elements 16, 381-387.
17. Fabrichnaya, O.B., 1999. The phase relations in the FeO-MgO-Al2O3-SiO2 system: assessment of thermodynamic properties and phase equilibria at pressures up to 30 GPa. Calphad, 23, 19-67.
18. Ferré, E.C., Friedman, S.A., Martín-Hernández, F., Feinberg, J.M., Conder, J.A., Ionov, D.A., 2013. The magnetism of mantle xenoliths and potential implications for sub-Moho magnetic sources. Geophys. Res. Lett. 40, 105–110.

766 19. Frezzotti, M.L., Touret, J.L.R., Lustenhouwer, W.J., Neumann, E.R., 1994. Melt and
767 fluid inclusions in dunite xenoliths from La Gomera, Canary Islands: tracking the
768 mantle metasomatic fluids. Eur. J. Mineral. 6, 805-817.
769 20. Frost, B.R., Ballhaus, C., 1998. Comment on" Constraints on the origin of the oxidation
770 state of mantle overlying subduction zones: an example from Simcoe, Washington,
771 USA" by AD Brandon and DS Draper. Geochim. Cosmochim. Acta, 62, 329-332.
772 21. Fumagalli, P., Stixrude, L., Poli, S., Snyder, D., 2001. The 10 phase: a high-pressure
773 expand- able sheet silicate stable during subduction of hydrated lithosphere. Earth
774 Planet. Sci. Lett. 186, 125–141.
775 22. Holland, T.J.B., Powell, R.T.J.B., 1998. An internally consistent thermodynamic data
776 set for phases of petrological interest. J. Metamorph. Geol., 16, 309-343.
777 23. Holland, T.J., Hudson, N.F., Powell, R., Harte, B., 2013. New thermodynamic models
778 and calculated phase equilibria in NCFMAS for basic and ultrabasic compositions
779 through the transition zone into the uppermost lower mantle. J. Petrol., 54, 1901-1920.
780 24. Hwang S-L., Yui, T-F., Chu, H-T., Shen, P., Iizuka, Y., Yang, H-Y., Yang, J., Xu, Z.,
781 2008. Hematite and magnetite precipitates in olivine from the Sulu peridotite: A result
782 of dehydrogenation-oxidation reaction of mantle olivine? Am. Min. 93, 1051-1060.
783 25. Iacovino, K., Guild, M.R., Till, C.B., 2020. Aqueous fluids are effective oxidizing
784 agents of the mantle in subduction zones. Contrib. Milneral. Petrol. 175: 36.
785 26. Kelley, K.A., Cottrell, E. 2009. Water and the oxidation state of subduction zone
786 magmas. Science, 325, 605–607.
787 27. Klein F., Bach W., McCollom T.M., 2013. Compositional controls on hydrogen
788 generation during serpentinization of ultramafic rocks. Lithos, 178, 55-69.
789 28. Laborda-López C., López Sánchez-Vizcaíno V., Marchesi C., Gómez-Pugnaire M. T.,
790 Garrido C. J., Jabaloy-Sánchez A., Padrón-Navarta J. A., Hidas, K., 2018. High-P

791 metamorphism of rodingites during serpentinite dehydration (Cerro del Almirez,
792 Southern Spain): Implications for the redox state in subduction zones. J. Metam. Geol.,
793 36, 1141-1173.
794 29. Lamadrid, H.M., Rimstidt, J.D., Schwarzenbach, E.M., Klein, F., Ulrich, S., Dolocan,
795 A., Bodnar, R.J., 2017. Effect of water activity on rates of serpentinization of
796 olivine. Nature Comm., 8, 16107.
797 30. Lyubutin, I.S., Lin, C.R., Korzhetskiy, Y.V., Dmitrieva, T.V., Chiang, R.K., 2009.
798 Mössbauer spectroscopy and magnetic properties of hematite/magnetite
799 nanocomposites. J. Appl. Phys., 106, 034311.
800 31. Macwell, S.J., 1992. Oxidation kinetics of fayalite (Fe2SiO4): Phys. Chem. Mineral.
801 19, 220-228.
802 32. Malaspina, N., Alvaro, M., Campione, M., Wilhelm, H., Nestola, F., 2015. Dynamics
803 of mineral crystallization from precipitated slab-derived fluid phase: first in situ
804 synchrotron X-ray measurements. Contrib. Mineral. Petrol., 169, 1-12.
805 33. Malaspina, N., Hermann, J., Scambelluri, M., 2009b. Fluid/mineral interaction in UHP
806 garnet peridotite. Lithos 107, 38-52.
807 34. Malaspina, N., Hermann, J., Scambelluri, M., Compagnoni, R., 2006. Polyphase
808 inclusions in garnet–orthopyroxenite (Dabie Shan, China) as monitors for
809 metasomatism and fluid-related trace element transfer in subduction zone
810 peridotite. Earth Planet. Sci. Lett., 249(3-4), 173-187.
811 35. Malaspina, N., Langenhorst, F., Tumiati, S., Campione, M., Frezzotti, M. L., Poli, S.,
812 2017. The redox budget of crust-derived fluid phases at the slab-mantle
813 interface. Geochim. Cosmochim. Acta, 209, 70-84.
814 36. Malaspina, N., Langenhorst, F., Tumiati, S., Fumagalli, P., Tumiati, S., Poli, S., 2012.
815 Fe3+ distribution between garnet and pyroxenes in mantle wedge carbonate-bearing

816 garnet peridotites (Sulu, China) and implications for their oxidation state. Lithos, 146,
817 11-17.
818 37. Malaspina, N., Poli, S., Fumagalli, P., 2009a. The oxidation state of metasomatized
819 mantle wedge: insights from C–O–H-bearing garnet peridotite. J. Petrol., 50, 1533-
820 1552.
821 38. Malaspina, N., Scambelluri, M., Poli, S., Van Roermund, H. L. M., Langenhorst, F.,
822 2010. The oxidation state of mantle wedge majoritic garnet websterites metasomatised
823 by C-bearing subduction fluids. Earth Planet. Sci. Lett., 298, 417-426.
824 39. Malaspina, N., Tumiati, S., 2012. The role of COH and oxygen fugacity in subduction-
825 zone garnet peridotites. Eu. J. Mineral., 24, 607-618.
826 40. Manning, C.E., Antignano, A., Lin, H.A. 2010. Premelting polymerization of crustal
827 and mantle fluids, as indicated by the solubility of albite+ paragonite+ quartz in H2O at
828 1 GPa and 350–620 °C. Earth Planet. Sci. Lett. 292, 325-336.
829 41. Maurice, J., Bolfan-Casanove, N., Demouchy, S., Chauvigne, P., Schiavi, F., Debret, B.
830 2020. The intrinsic nature of antigorite breakdown at 3 GPa: Experimental constraints
831 on redox conditions of serpentinite dehydration in subduction zones. Contrib. Mineral.
832 Petrol. 175: 94.
833 42. Moine, B.N., Bolfan-Casanova, N., Radu, I.B., Ionov, D.A., Costin, G., Korsakov, A.V.,
834 Golovin, A.V., Oleinikov, O.B., Deloule, E., Cottin, J.Y., 2020. Molecular hydrogen in
835 minerals as a clue to interpret ∂D variations in the mantle. Nature Commun., 11, 1-10.
836 43. Merkulova, M.V., Muñoz, M., Brunet, F., Vidal, O., Hattori, K., Vantelon, D., Trcera,
837 N., Huthwelker, T. 2017. Experimental insight into redox transfer by iron-and sulfur-
838 bearing serpentinite dehydration in subduction zones. Earth Planet. Sci. Lett. 479, 133-
839 143.

840 44. Mungall, J.E. 2002. Roasting the mantle: Slab melting and the genesis of major Au and
841 Au-rich Cu deposits. Geology, 30, 915-918.
842 45. Oglialoro, E., Frezzotti, M., Ferrando, S., Tiraboschi, C., Principe, C., Groppelli, G.,
843 Villa, I., 2017. Lithospheric magma dynamics beneath the El Hierro Volcano, Canary
844 Islands: insights from fluid inclusions. Bull. Volcanol. 79.
845 46. Osborne, M. D., Fleet, M.E., Bancroft, G.M., 1981. Fe2+-Fe3+ ordering in Chromite
846 and Cr-bearing Spinels. Contrib. Mineral. Petrol. 77, 251-255.
847 47. Oyama, S.T., Wang, X., Lee, Y.K., Chun, W.J., 2004. Active phase of Ni2P/SiO2 in
848 hydroprocessing reactions. J. Catal., 221(2), 263-273.
849 48. Padrón-Navarta, J.A., Hermann, J., Garrido, C. J., López López Sánchez-Vizcaíno, V.,
850 Gómez-Pugnaire, M.T., 2010. An experimental investigation of antigorite dehydration
851 in natural silica-enriched serpentinite. Contrib. Mineral. Petrol., 159, 25-42.
852 49. Padrón-Navarta, J.A., Sanchez-Vizcaino, V., Garrido, C. J., Gómez-Pugnaire, M. T.,
853 2011. Metamorphic record of high-pressure dehydration of antigorite serpentinite to
854 chlorite harzburgite in a subduction setting (Cerro del Almirez, Nevado–Filábride
855 Complex, Southern Spain). J. Petrol., 52, 2047-2078.
856 50. Padrón-Navarta, J.A., López Sánchez-Vizcaíno, V.L., Hermann, J., Connolly, J.A.,
857 Garrido, C.J., Gómez-Pugnaire, M.T., Marchesi, C., 2013. Tschermak's substitution in
858 antigorite and consequences for phase relations and water liberation in high-grade
859 serpentinites. Lithos, 178, 186-196.
860 51. Peng, W., Zhang, L., Tumiati, S., Vitale Brovarone, A., Hu, H., Cai, Y., Shen, T., 2020.
861 Abiotic methane generation through reduction of serpentinite-hosted dolomite:
862 implications for carbon mobility in subduction zones. Geochim. Coosmochim. Acta,
863 311, 119-140.

52. Petriglieri, J.R., Salvioli-Mariani, E., Mantovani, L., Tribaudino, M., Lottici, P.P., Laporte-Magoni, C., Bersani, D. 2015. Micro-Raman mapping of the polymorphs of serpentine. J. Raman Spec, 46, 953-958.

53. Piccoli, F., Hermann, J., Pettke, T., Connolly, J.A.D., Kempf, E.D., Vieira Duarte, J.F., 2019. Subducting serpentinites release reduced, not oxidized, aqueous fluids. Sci. Rep., 9(1), 1-7.

54. Pitzer, K.S., Sterner, S.M., 1994. Equations of state valid continuously from zero to extreme pressures for H2O and CO2. The Journal of chemical physics 101.4, 3111-3116.

55. Poli, S. 2015. Carbon mobilized at shallow depths in subduction zones by carbonatitic liquids. Nature Geosci. 8, 633-636.

56. Potapkin, V., Chumakov, A.I., Smirnov, G. V., Celse, J.P., Rüffer, R., McCammon, C., Dubrovinsky, L., 2012. The 57Fe synchrotron Mössbauer source at the ESRF. J. Synchro. Rad., 19, 559-569.

57. Prescher, C., McCammon, C., Dubrovinsky, L., 2012. MossA: a program for analyzing energy-domain Mössbauer spectra from conventional and synchrotron sources. J. Appl. Crystal., 45, 329-331.

58. Puga, E., Nieto, J. M., de Federico, A. D., Bodinier, J. A., Morten, L., 1999. Petrology and metamorphic evolution of ultramafic rocks and dolerite dykes of the Betic Ophiolitic Association (Mulhacén Complex, SE Spain): evidence of eo-Alpine subduction following an ocean-floor metasomatic process. Lithos, 49, 23-56.

59. Rooney, J.S., Tarling, M. S., Smith, S. A., & Gordon, K. C. (2018). Submicron Raman spectroscopy mapping of serpentinite fault rocks. Journal of Raman Spectroscopy, 49(2), 279-286.

888 60. Ruiz Cruz, M.R., Puga, E., Nieto, J.M., 1999. Silicate and oxide exsolution in pseudo-
889 spinifex olivine from metaultramafic rocks of the Betic Ophiolitic Association; a TEM
890 study. Am. Mineral., 84, 1915-1924.
891 61. Rüffer, R., Chumakov, A.I., 1996. Nuclear resonance beamline at ESRF. Hyper.
892 Interac., 97, 589-604.
893 62. Sánchez-Vizcaíno, V.L., Rubatto, D., Gómez-Pugnaire, M.T., Trommsdorff, V.,
894 Müntener, O., 2001. Middle Miocene high-pressure metamorphism and fast exhumation
895 of the Nevado-Filábride Complex, SE Spain. Terra Nova, 13, 327-332.
896 63. Scambelluri, M., Bottazzi, P., Trommsdorff, V., Vannucci, R., Hermann, J., Gòmez-
897 Pugnaire, M. T., Vizcaìno, V.L.S., 2001. Incompatible element-rich fluids released by
898 antigorite breakdown in deeply subducted mantle. Earth Planet. Sci. Lett., 192, 457-
899 470.
900 64. Scambelluri, M., Müntener, O., Ottolini, L., Pettke, T. T., Vannucci, R., 2004. The fate
901 of B, Cl and Li in the subducted oceanic mantle and in the antigorite breakdown
902 fluids. Earth Planet. Sci. Lett., 222, 217-234.
903 65. Scambelluri, M., Pettke, T., Cannaò, E., 2015. Fluid-related inclusions in Alpine high-
904 pressure peridotite reveal trace element recycling during subduction-zone dehydration
905 of serpentinized mantle (Cima di Gagnone, Swiss Alps). Eart Planet. Sci. Lett. 429, 45-
906 59.
907 66. Scambelluri, M. Piccardo, G.B., Philippot, P., Robbiano, A., Negretti. L., 1997. High
908 salinity fluid inclusions formed from recycled seawater in deeply subducted alpine
909 serpentinite. Earth Planet. Sci. Lett. 148, 485-499.
910 67. Schmidt, B. C., Holtz, F.M., Beny, J.M., 1998. Incorporation of H2 in vitreous silica,
911 qualitative and quantitative determination from Raman and infrared spectroscopy. J.
912 Non-crystal. Solids., 240, 91-103.

913 68. Shebanova, O.N., Lazor, P., 2003. Raman spectroscopic study of magnetite (FeFe2O4):
914 a new assignment for the vibrational spectrum. J. Solid State Chem. 174, 424-430.
915 69. Tiraboschi, C., McCammon, C., Rohrbach, A., Klemme, S., Berndt, J., Sanchez-Valle,
916 C. 2023. Preferential mobilisation of oxidised iron by slab-derived hydrous silicate
917 melts. Geochem. Persp. Lett., 24, 43-47.
918 70. Tiraboschi, C., Tumiati, S., Recchia, S., Miozzi, F., Poli, S., 2016. Quantitative analysis
919 of COH fluids synthesized at HP–HT conditions: an optimized methodology to measure
920 volatiles in experimental capsules. Geofluids, 16(5), 841-855.
921 71. Tropper, P., Manning, C.E., 2007. The solubility of corundum in H2O at high pressure
922 and temperature and its implications for Al mobility in the deep crust and upper
923 mantle. Chem. Geol., 240, 54-60.
924 72. Tumiati, S., Fumagalli, P., Poli, S. 2013. An experimental study on COH-bearing
925 peridotite up to 3· 2 GPa and implications for crust–mantle recycling. J. Petrol., 54, 453-
926 479.
927 73. Tumiati, S., Godard, G., Martin, S., Malaspina, N., Poli, S., 2015. Ultra-oxidized rocks
928 in subduction mélanges? Decoupling between oxygen fugacity and oxygen availability
929 in a Mn-rich metasomatic environment. Lithos, 226, 116-130.
930 74. Tumiati, S., Malaspina, N., 2019. Redox processes and the role of carbon-bearing
931 volatiles from the slab–mantle interface to the mantle wedge. J. Geol. Soc. 176, 388-
932 397.
933 75. Tumiati, S., Tiraboschi, C., Sverjensky, D.A., Pettke, T., Recchia, S., Ulmer, P., Miozzi,
934 F. Poli, S. (2017). Silicate dissolution boosts the CO2 concentrations in subduction
935 fluids. Nature Commun. 8, 1-11.
936 76. Tumiati, S., Recchia, S., Remusat, L., Tiraboschi, C., Sverjensky, D.A., Manning, C.
937 E., Vitale Brovarone A., Boutier, A., Spanu, D., Poli, S., 2022. Subducted organic

matter buffered by marine carbonate rules the carbon isotopic signature of arc emissions. Nature Commun. 13, 1-10.

77. Trommsdorff, V., López Sánchez-Vizcaíno, V.L., Gómez-Pugnaire, M.T., Müntener, O., 1998. High pressure breakdown of antigorite to spinifex-textured olivine and orthopyroxene, SE Spain. Contrib. Mineral. Petrol., 132, 139-148.
78. Ulmer, P., Trommsdorff, V., 1995. Serpentine stability to mantle depths and subduction-related magmatism. Science, 268, 858-861.
79. Vieira Duarte, J. F., Piccoli, F., Pettke, T., Hermann, J., 2021. Textural and geochemical evidence for magnetite production upon antigorite breakdown during subduction. J. Petrol., 62, egab053.
80. Vitale Brovarone, A., Sverjensky, D. A., Piccoli, F., Ressico, F., Giovannelli, D., Daniel, I., 2020. Subduction hides high-pressure sources of energy that may feed the deep subsurface biosphere. Nature Commun. 11, 1-11.
81. Zelenski, M., Plyasunov, A.V., Kamenetsky, V.S., Nekrylov, N., Matveev, D., Korneeva, A., 2022. High-temperature water–olivine interaction and hydrogen liberation in the subarc mantle. Contrib. Mineral. Petrol. 177, 1-21.